

Direct detection of coupled proton and electron transfers in human manganese superoxide dismutase

Jahaun Azadmanesh

University of Nebraska Medical Center

William Lutz

University of Nebraska Medical Center

Leighton Coates

Oak Ridge National Laboratory <https://orcid.org/0000-0003-2342-049X>

Kevin Weiss

Oak Ridge National Laboratory <https://orcid.org/0000-0002-6486-8007>

Gloria Borgstahl (✉ gborgstahl@unmc.edu)

University of Nebraska Medical Center <https://orcid.org/0000-0001-8070-0258>

Article

Keywords: concerted proton and electron transfers (CPETs), human manganese superoxide dismutase (MnSOD), glutamine deprotonation

Posted Date: November 11th, 2020

DOI: <https://doi.org/10.21203/rs.3.rs-101621/v1>

License:  This work is licensed under a Creative Commons Attribution 4.0 International License.

[Read Full License](#)

Version of Record: A version of this preprint was published at Nature Communications on April 6th, 2021. See the published version at <https://doi.org/10.1038/s41467-021-22290-1>.

Direct detection of coupled proton and electron transfers in human manganese superoxide dismutase

Jahaun Azadmanesh,¹ William E. Lutz,² Leighton Coates,³ Kevin L. Weiss,⁴ and Gloria E. O. Borgstahl^{1,2}

¹Department of Biochemistry and Molecular Biology, 985870 Nebraska Medical Center, Omaha, NE 68198-5870, USA

²Eppley Institute for Cancer and Allied Diseases, 986805 Nebraska Medical Center, Omaha, NE 68198-6805, USA

³Second Target Station, Oak Ridge National Laboratory, 1 Bethel Valley Road, Oak Ridge, TN 37831, USA

⁴Neutron Scattering Division, Oak Ridge National Laboratory, 1 Bethel Valley Road, Oak Ridge, TN 37831, USA

Abstract

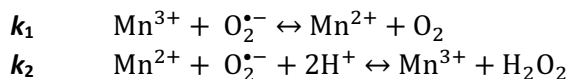
Human manganese superoxide dismutase (MnSOD) is a critical oxidoreductase found in the mitochondrial matrix. Concerted proton and electron transfers (CPETs) are used by the enzyme to rid the mitochondria of $O_2^{\cdot-}$, a precursor to other harmful reactive oxygen and nitrogen species. The mechanisms of CPET-utilizing enzymes are typically unknown due to the difficulties in detecting the protonation states of specific residues and solvent molecules involved in catalysis while controlling the redox state of the enzyme. Here, neutron diffraction of redox-controlled MnSOD crystals revealed the all-atom structures of Mn^{3+} SOD and Mn^{2+} SOD delivering unique data on sites of differential protonation. A novel mechanism is proposed from the direct observation of glutamine deprotonation, the involvement of Tyr and His with altered pK_{as} , and three unusual strong-short hydrogen bonds that change with the oxidation state of the metal. Quantum calculations provide insight into the electronic modulation of the observed structures.

Introduction

Oxidoreductases are a large class of enzymes that use unpaired electrons to facilitate redox reactions with other chemical species and are involved in nearly all aspects of life. Oxidoreductase electron transfers are almost always coupled with a proton transfer¹. Concerted proton and electron transfer (CPET) permits a thermodynamically favorable redox reaction that avoids ionized intermediates, is extremely efficient, and is an integral part of enzymes with the fastest catalytic rates²⁻⁴. Particularly noteworthy is the prominence of CPET enzymes that regulate the concentration of reactive oxygen species (ROS) in the cell. ROS levels are central to programmed cell death and abnormal regulation by these oxidoreductases play significant roles in cancer and cardiovascular diseases⁵. CPETs are therefore of significant interest to study but a mechanistic understanding of these enzymes is still lacking. Deciphering these fundamental biochemical reactions is not only significant for its role in diseases, but for the biomedical design of CPET-dependent therapeutic interventions, irradiation protectants, and electrochemical biosensors^{6,7}.

Human MnSOD is a CPET-based oxidoreductase found in the mitochondrial matrix that reduces ROS levels by eliminating $O_2^{\cdot-}$ with the unpaired electrons of the active site metal. The Mn is coordinated to inner-sphere residues His26, His74, His163, Asp159, and a single-oxygen

species that could be either H₂O or ⁻OH (designated WAT1, Fig. 1). Trivalent Mn oxidizes O₂^{•-} to O₂ ($k_1 = 1.5 \text{ nM}^{-1}\text{s}^{-1}$) and the resulting divalent Mn reduces another O₂^{•-} molecule to H₂O₂ ($k_2 = 1.1 \text{ nM}^{-1}\text{s}^{-1}$)⁸. This is the only means the mitochondrial matrix has to keep O₂^{•-} levels low enough to avoid damage to macromolecules and cellular function⁹.



The major endogenous source of O₂^{•-} is from electrons inadvertently leaking from the electron transport chain. Dysfunctional MnSOD activity, therefore, poses significant consequences on the mitochondria that contributes to several diseases. Genetic aberrations of MnSOD are associated with several cancer types, with mammary and prostate cancers being the most frequently noted in curated databases¹⁰. Polymorphisms of MnSOD have also been noted to be a predictor for deficient vascular function¹¹. Therefore, the ability of MnSOD to utilize the high reaction rate and efficiency ($k_{\text{cat}}/K_m > \sim 10^9 \text{ M}^{-1}\text{s}^{-1}$) of its CPET mechanism is correlated with the preservation of health⁸.

The CPET mechanism of MnSOD, and the majority of other oxidoreductases, has yet to be defined at the atomic level. The limitation in studying CPETs is the difficulty in directly detecting the protonation states of ionizable residues, solvent/ligands at the active site, and correlating them with the electronic state of the active site metal. The second-sphere of MnSOD harbors five residues (His30, Tyr34, Gln143, Glu162, and Tyr166; Fig. 1) and information about their protonation states would be of significant value in deciphering a catalytic mechanism. X-ray and spectroscopic techniques have been unable to provide this information due to the poor scattering of hydrogen atoms and the difficulty in discerning spectra for specific titratable positions. Neutron protein crystallography (NPC) is an emerging tool for analyzing hydrogen positions of biological macromolecules and possesses attributes that are especially useful in deciphering CPET mechanisms. In NPC, scattering of deuterium is on par with carbon, nitrogen, and oxygen, significantly increasing the ability to locate proton positions for the entire enzyme. An additional advantage is that neutrons do not alter the electronic state of metals, unlike X-rays¹³. Here, we present room temperature neutron structures of human MnSOD at physiological pH in Mn³⁺ and Mn²⁺ and reveal how the atomic locations of all protons in the enzyme active

site exchange when the active site metal goes through a redox cycle. To our knowledge, this study provides the first direct experimental evidence of a CPET enzymatic mechanism.

Results and Discussion

Direct evidence for CPETs at the active site metal with a previously unpredicted glutamine deprotonation

To visualize the effect of the electronic state of the metal on the active site protons, all-atom neutron structures were obtained for Mn³⁺SOD and Mn²⁺SOD to resolutions of 2.20 and 2.30 Å, respectively. The two data sets collected were from the same perdeuterated crystal treated with first an oxidizing agent and then reducing chemicals. The redox conditions were maintained during each data collection¹⁴. Neutron data at these resolutions is excellent and permitted ease in the visualization of deuterium atoms. The proton structure of the two active sites without O₂⁻ were specifically sought to define the effects of metal redox state independent of substrate binding. We initially sought a crystallographic “check” for the success of the redox manipulations. WAT1 has historically been thought to obtain a proton (⁻OH → HOH) upon one-electron reduction of Mn³⁺ to Mn²⁺ for a CPET reaction but had not yet been directly observed and confirmed^{4,15-22}. Indeed, careful inspection of the nuclear density between both neutron data sets suggested differential protonation of the WAT1 Mn-ligand dependent on the redox state of the Mn (Fig. 2a-b). This was theoretically expected, verified our methods, and gave confidence in the data. To our knowledge, this is the first time the chemical reduction of the metal was visually observed to change the protonation state of an active site ligand.

For Mn³⁺SOD, a single nuclear |F_o|-|F_c| density peak for the D¹ atom of WAT1 is seen suggesting the expected deuterioxide (⁻OD) molecule and is supported by the Mn-O(WAT1) distance of 1.8 Å^{23,24}. The ⁻OD acts as a hydrogen bond donor to the O^{ε2} of Asp159 with a distance of 2.1 Å whereas the O(WAT1) atom is acting as a hydrogen bond acceptor from D^{ε21}(Gln143) with a distance of 1.8 Å (Fig. 2a). The data for WAT1 of Mn²⁺SOD instead has two nuclear |F_o|-|F_c| density peaks for D atoms indicating the ⁻OD was converted to D₂O upon metal reduction, as expected. Further support suggesting a D₂O molecule is seen with the Mn-O(WAT1) distance of 2.2 Å^{23,24}. The D¹(WAT1) atom position is similar to that found in the Mn³⁺SOD counterpart and hydrogen bonds with O^{ε2} of Asp159, albeit at a weaker interaction of 2.5 Å distance (Fig. 2b). Surprisingly, D²(WAT1) points toward Gln143 suggesting the WAT1

of Mn^{2+} SOD is acting as a hydrogen bond donor to Gln143. This means Gln143 is a hydrogen bond acceptor in Mn^{2+} SOD and its $\text{D}^{\epsilon 21}$ atom is absent. Indeed, there is a lack of nuclear density for $\text{D}^{\epsilon 21}$ but not for $\text{D}^{\epsilon 22}$. This interpretation was supported when attempts to model $\text{D}^{\epsilon 21}$ led to negative $|\text{F}_o| - |\text{F}_c|$ nuclear density. In the Mn^{2+} SOD structure the hydrogen bond between $\text{D}^2(\text{WAT1})$ and $\text{N}^{\epsilon 2}(\text{Gln143})$ is atypical with a bond distance of only 1.6 Å and $\text{O}(\text{WAT1}) - \text{D}^2(\text{WAT1}) - \text{N}^{\epsilon 2}(\text{Gln143})$ angle close to 180° . These are characteristics of a short-strong hydrogen bond (SSHB), a type of hydrogen bond that is thought to stabilize particular enzymatic steps and enhance catalytic rates²⁵⁻²⁷. SSHBs are noteworthy in several well-studied enzymes, such as α -chymotrypsin that utilizes a SSHB between the His and Asp of its catalytic triad²⁶. This creates a ~ 7 kcal/mol stronger interaction to substantially increase the kinetic rate. For Mn^{2+} SOD, the SSHB between WAT1 and Gln143 may contribute to the stability of the unusual redox state and the high catalytic efficiency of the enzyme.

The experimental data, therefore, suggest that Gln143 is undergoing deprotonation to form an amide anion and is especially unusual because glutamine residues are not expected to act as weak acids since the pK_a of primary amides are 16 \sim 18. However, pK_a studies of less acidic secondary amides suggest pK_a values may be depressed to 7 \sim 8 depending on how the amide group is polarized (i.e. charge delocalization)²⁸. This is supported by the known event of proton exchanges occurring at the amide groups of protein backbones. Moreover, several enzyme studies suggest glutamine or asparagine-mediated proton transfers for catalysis and support the plausibility of a Gln143 \rightarrow WAT1 proton transfer. For example, an asparagine residue has been suggested to be deprotonated in prenyltransferases due to significant polarization from close proximity to a metal cation²⁹. Nakamura and colleagues showed neutron data of cellulase Cel45A from *Phanerochaete chrysosporium* that revealed asparagine deprotonation that is instrumental for the proton relay of the enzyme³⁰. Infrared spectroscopy and computational calculations support the involvement of glutamine-mediated proton transfers in GTP hydrolysis by Ras-GAP and photoexcitation of photoreceptor proteins with the flavin-binding BLUF domain³¹. For MnSOD, the deprotonation of Gln143 for CPET to the active site ligand has not been observed before although it does explain the extremely high efficiency of the enzyme as a result of this internal proton source.

Density functional theory (DFT) quantum calculations of the active site using the neutron structures support our interpretation of the nuclear density for deprotonation of Gln143. Calculations used the atoms of the residues shown in Fig. 1. Chemist's localized property-optimized orbital (CLPO) analysis (highly akin to Natural Bond Orbitals³²⁻³⁴) was used to evaluate the interactions of Gln143 and WAT1³⁵. Reduction of Mn^{3+} to Mn^{2+} increases the electronegative character of the O(WAT1) lone pair facing the proximal amide proton of Gln143 (green atom, Fig. 3a). This polarization of OH(WAT1) increases its basicity chemically allowing the abstraction of the amide proton from glutamine. In this way, a hard acid-hard base interaction ($\text{Mn}^{3+}\text{-OH}$) has become a soft acid-soft base ($\text{Mn}^{2+}\text{-OH}_2$) interaction. The bonds of the deprotonated amide reorganize to stabilize its new negatively-charged state (Fig. 3b). The $\text{O}^{\epsilon 1}$ atom of Gln143 bears the most electronegative charge, and calculations suggest less covalent electrons for the $\text{O}^{\epsilon 1}\text{-C}^{\epsilon 1}$ bond compared to that of $\text{N}^{\epsilon 2}\text{-C}^{\epsilon 1}$, with bond orders of 1.33 and 1.52, respectively (Table S1). The presence of a SSHB is supported as well since the deprotonated $\text{N}^{\epsilon 2}$ still has covalent character with the donated proton D^2 (Fig. 3c). Donor-acceptor orbital analysis indicates electron density is transferred from the $\text{N}^{\epsilon 2}$ lone pair orbital to the σ^* -antibonding orbital of O-H(WAT1) and is a 1.4 kcal/mol stabilizing hyperconjugation interaction (Table S2). As a result, the interaction between $\text{N}^{\epsilon 2}$ and the donated proton demonstrates partial σ -bonding character. The extent of covalence is 36% for the $\text{N}^{\epsilon 2}\text{-H}$ bond and 64% for the O-H bond (Table S3). Altogether, quantum calculations support both Gln143 deprotonation and the presence of an unusual hydrogen bond between WAT1 and Gln143.

A previously undetected change in the interaction of Gln143 with the neighboring Trp123 was observed. A SSHB of 1.5 Å is seen between the $\text{O}^{\epsilon 1}$ of Gln143 and $\text{D}^{\epsilon 1}$ of Trp123 (Fig. 2b). The same hydrogen bond is seen in Mn^{3+}SOD at a distance of 1.9 Å (Fig. 2a). The neutron data, therefore, support the notion that $\text{O}^{\epsilon 1}(\text{Gln143})$ harbors stronger electronegative character during the Mn^{2+} redox state. This may be a consequence of Gln143 deprotonation to the amide anion during the $\text{Mn}^{3+} \rightarrow \text{Mn}^{2+}$ redox reaction and negative charge stabilization through hydrogen bonding with Trp123. Charge stabilization is likely to be important for glutamine deprotonation as amide groups are known to deprotonate at neutral pH when electronegatively polarized at the carbonyl O atom²⁸. Trp123 is especially competent at charge stabilization due to its own ability to polarize. CLPOs suggest that lone pair electrons of $\text{N}^{\epsilon 1}(\text{Trp123})$ delocalize into the highly-conjugated aromatic ring of Trp123 when the glutamine amide is deprotonated and is stabilizing

(Fig. 3e). Donor-acceptor orbital analysis calculate that the major stabilizing interaction is the donation of N^{ε1}(Trp123) lone pair electron density into the C^{ε2}-C^{δ2} π*-antibonding orbital (Fig. 3f) and decreases energy by 13.52 kcal/mol (Table S2). This also permits the observation of close hydrogen bond interaction between O^{ε1}(Gln143) and H^{ε1}(Trp123). Quantum calculations indicate an important role for Trp123 in the deprotonation of Gln143.

If an O(WAT1)-D^{ε21}(Gln143)- N^{ε2}(Gln143) interaction is needed for redox cycling of Mn, mutation of Gln143 or a nearby residue that may stabilize amide deprotonation should affect catalysis. In the literature, the Gln143Asn mutant has nearly ablated catalysis in both redox states while Trp123Phe can perform catalysis for Mn³⁺ → Mn²⁺ at deficient lower rates (20 ~ 50 %) but not at all for the Mn²⁺ → Mn³⁺ transition^{36,37}. The effect of these mutations suggests that Gln143 is central to catalytic activity while Trp123 is most significant for the Mn²⁺ → Mn³⁺ half of the redox cycle. The detrimental effects for the Mn²⁺ state due to mutating residue Trp123 may therefore reflect their role in stabilizing the Gln143 amide anion. Indeed, the kinetic behaviors of these mutants were especially puzzling in past studies but amide proton transfer potentially explains them³⁷⁻⁴⁰. A glutamine at the position of Gln143 is conserved in all isoforms of MnSODs and prokaryotic FeSODs and a closer WAT1-Gln distance correlates with increased redox potentials and catalytic rates⁴¹. This is perhaps because of an enhanced ability for proton transfers between O(WAT1) and N^{ε2}(Gln143). Past mutagenesis studies, differences in catalytic rates among isoforms, and the high catalytic rate of MnSOD may be explained by Gln143 serving as an internal proton source for CPET via amide deprotonation.

Tyr34 demonstrates an unusual pK_a and forms a SSHB with the Gln143 amide anion

Tyr34 is positioned near the active site solvent channel, hydrogen-bonded to Gln143 (Fig. 1a), and has been hypothesized to be a proton source for MnSOD CPET⁴⁰. For Mn³⁺SOD, Tyr34 does not have a nuclear peak for its hydroxyl proton. Deprotonated Tyr34 is making a very strong hydrogen bond with a nearby solvent molecule (designated WAT2) with a 2.3 Å distance between heteroatoms Oⁿ(Tyr34) and O(WAT2) (Fig. 4a). While the deuteriums of WAT2 could not be discerned, the distance is characteristic of a SSHB where Tyr34 may be poised to accept a proton. This interpretation is supported by CLPO analysis from DFT, with 80/20 covalent sharing of the proton (Table S3). For Mn²⁺SOD, a nuclear peak for the hydroxyl proton is present but not where it is expected. Refinement with the ideal 0.97 Å Oⁿ-Dⁿ distance for Tyr34

persistently demonstrates residual $|F_o|-|F_c|$ difference density (Fig. S1) uncharacteristic of the other MnSOD tyrosine residues. Between refinement, restraints for this Tyr34 were incrementally loosened from the 0.97 Å ideal hydroxyl distance until the $|F_o|-|F_c|$ difference density was appropriately absent and the B factors were comparable to other nearby atoms. This yielded an unusual Oⁿ-Dⁿ bond length of 1.3 Å that points towards the solvent channel (Fig. 4b). Intriguingly, the Oⁿ(Tyr34) atom participates in a strong 1.6 Å hydrogen bond with D^{e22}(Gln143) in the Mn²⁺SOD structure and is significantly different than the Mn³⁺SOD distance of 2.3 Å (Fig. 4a-b). This SSHB may potentially be explained by the increased polarization of Gln143 in Mn²⁺SOD from deprotonation to the amide anion leading to a stronger hydrogen bond interaction with Tyr34. It is unclear whether this interaction contributes to Tyr34 differential protonation though it may stabilize the amide anion of Gln143. The experimental data, therefore, suggest Tyr34 is capable of differential protonation at physiological pH, has an unusual pK_a, and participates in atypical hydrogen bonding.

Our experimental data for Tyr34 potentially shines light on the unexplained observations of previous studies investigating its role in catalysis^{8,37,40}. Tyr34 has been speculated to be the proton donor to WAT1 for CPET during the Mn³⁺ → Mn²⁺ reaction though this conflicts with the pH independence of the reaction between values of 6 and 10^{8,42}. This was puzzling because CPET mechanisms are expected to have pH dependence as a result of the proton transfer part of their catalysis and Tyr34 is the closest titratable residue. Instead, the MnSOD neutron data suggest that the proton donor to WAT1 is internally sourced from Gln143 without the direct involvement of solvent and cannot be Tyr34 due to its observed deprotonation in the Mn³⁺ state.

An ionized tyrosine residue at physiological pH is unusual though has been visualized in studies of human carbonic anhydrase II (HCA II) a metalloenzyme with diffusion-limited catalytic efficiencies like MnSOD. For HCA II, joint neutron crystallography and NMR demonstrate a tyrosine residue with a pK_a of 7.10 ± 0.10 at the active site⁴³. The catalytic role of an ionizable Tyr34 for MnSOD is prominent during the Mn²⁺ → Mn³⁺ redox cycle and is supported by the inability of the Tyr34Phe mutant to catalyze this step of the reaction⁴⁴. Since Tyr34 gains a proton during the Mn³⁺ → Mn²⁺ redox cycle and loses a proton during the Mn²⁺ → Mn³⁺ cycle, it is conceivable that Tyr34 serves as the source for one of the two protons involved in the protonation of the substrate to H₂O₂. Indeed, spectroscopic data of the Tyr34Phe mutant

suggests a prolonged binding of a species to the metal but could also be a result of the inability of Gln143 to deprotonate without stabilization from the Tyr34 hydroxyl group⁴⁰. Our crystallographic neutron data has shed new light on the perplexing role of the conserved Tyr34 residue.

Serendipitous ligand binding to Mn²⁺SOD helps explain catalysis

There are two subunits in the crystallographic asymmetric unit (Fig. 1 inset, yellow and cyan chains) and one of the active sites of the Mn²⁺SOD neutron structure has density for a sixth-coordinate ⁻OD ligand (designated OL for anionic oxygen ligand, Fig. 4c). The 1.84 Å Mn-O distance of OL most closely supports a Mn²⁺ bound with ⁻OD¹⁶ and the B-factor of OL is comparable to other atoms of the active site. The different crystallographic active site coordination of Mn²⁺SOD may be a consequence of the crystallographic asymmetric subunits having different capacities of solvent accessibility (Fig. S2). Likewise, OL has been observed in two X-ray crystal structures of *E. coli* MnSOD by our group when ⁻OH was added to the buffer system and it was also not found in every active site^{45,46}. For the present study, the buffer system used for neutron data collection carefully did not include ⁻OD, and only appropriate ratios of K₂DPO₄ and KD₂PO₄ were used to achieve a pD equivalent to physiologically pH. We think the ligand may have resulted serendipitously from a polarized water molecule that lost a proton. Nevertheless, the bound sixth-coordinate ligand to the active site of Mn²⁺SOD chain A has a unique combination of structural characteristics that helps explain catalysis.

OL may help facilitate Gln143 amide deprotonation. The six-coordinate active site has a Gln143 in the canonical amide form making very strong hydrogen bonds with WAT1 and Trp123 that have bond distances of 1.4 and 1.5 Å, respectively (Fig. 4c). These distances are characteristic of SSHBs that may contribute to catalysis. Interestingly, the density of WAT1 is that of a hydroxide even though the Mn is stably reduced but likely has partial H₂O character given the shortness of the hydrogen bond with the nearby amide D^{ε21} proton. The Mn²⁺ protein-ligand bond lengths between the two active sites are not the same. In particular, the Mn-O^{ε2}(D159) bond is stretched from 1.95 to 2.44 Å when OL is bound (Table S4). This stretching supports the ‘associative-displacement’ mechanism predicted by Whittaker and coworkers who suggested that the association of a sixth-coordinate ligand displaces the aspartate from Mn⁴⁷. The D^{ε21}(Gln143) atom that bridges O(WAT1) and N^{ε2}(Gln143) has a slightly higher B-factor of 21

\AA^2 when compared to the B factors of 17\AA^2 for O(WAT1) and 18\AA^2 for $\text{N}^{\epsilon 2}$ (Gln143) and may reflect movement between O(WAT1) and $\text{N}^{\epsilon 2}$ (Gln143). Tyr34 is not protonated but appears poised to be protonated by WAT2 as indicated by a (D)WAT2-Oⁿ(Tyr34) bond distance of 1.7\AA . Binding by an anionic OL would lower the positive charge of Mn^{2+} and increasing the negative character of WAT1 to help initiate Gln143 amide deprotonation. In their investigation of active site pK_a s for MnSOD activity, the Miller group suggested sixth-coordinate binding of an OH^- ligand to the Mn^{2+} SOD active site at native conditions¹⁵. They hypothesize that an electronegative deprotonated Tyr34 and electropositive Mn could polarize a water molecule to have increased OH^- character and lose a proton. Since Tyr34 is deprotonated in the six-coordinate structure, proton abstraction from a water molecule likely occurs elsewhere, perhaps by nearby His30. As inferred by the five-coordinate Mn^{2+} SOD active site structure, subsequent catalytic steps involve OL leaving the active site, perhaps by protonation to water, and Tyr34 becoming protonated.

His30 demonstrates an unusual pK_a that is tied to Tyr166 from across the dimer interface

Second sphere residue His30 is also differentially protonated. Like Tyr34, His30 is solvent-exposed and positioned at the active site solvent channel. WAT2 provides a hydrogen-bond bridge between Tyr34 and His30 (Fig. 1a). Nuclear peaks of the neutron structures indicate differential protonation at the $\text{N}^{\delta 1}$ of His30 that faces the solvent channel for Mn^{3+} SOD (Fig. 5a-b). The crystallographic asymmetric unit has one active site with $\text{N}^{\delta 1}$ protonated while the other is not protonated. This is not the case for Mn^{2+} SOD, where both chains show nuclear density for $\text{N}^{\delta 1}$ protonation (Fig. S3). The hydrogen bond between His30 and Tyr166 for the Mn^{3+} SOD chain A active site (Fig. 5a) appears to have strong and elongated omit $|F_o| - |F_c|$ difference density for the D atom and this is the case for all active sites of Mn^{2+} SOD. This may suggest the presence of a SSHB with covalent but unequal sharing of the D atom between Oⁿ(Tyr166) and $\text{N}^{\epsilon 2}$ (His30) and/or movement of the D atom between the two residues. Since $\text{N}^{\epsilon 2}$ (His30) is solvent inaccessible along with the entirety of Tyr166 from across the dimer interface, the hydrogen bond between the residues is within an enclosed environment and may behave atypically compared to canonical hydrogen bonds.

For the active site absent of a proton at $\text{N}^{\delta 1}$ for His30 (Fig. 5b), the D atom between Oⁿ(Tyr166) and $\text{N}^{\epsilon 2}$ (His30) has a less $|F_o| - |F_c|$ difference density and appears covalent with

Oⁿ(Tyr166). His30 thus appears to not have protons at both of its nitrogens suggesting an imidazolate anion. We considered the presence of an imidazolate anion as chemically unlikely but deliberated over the possibility along with alternative explanations. The pK_a of [imidazole ↔ imidazolate] is 14 and compares with the pK_as of [HOH ↔ ·OH] and [HO-Tyr ↔ ·O-Tyr] that are 14 and 10, respectively⁴⁸. Since the electrostatic surface area encompassing and surrounding the active site is positively charged (Fig. 1a), it is conceivable that negatively-charged species are promoted. While it is known that active site residues have significantly perturbed pK_as due to such effects, we could not find literature suggesting an imidazolate histidine unless it is directly bound to a metal. Alternatively, His30 may shift between singly N^{δ1}- or N^{ε2}-protonated tautomers, and density may be absent due to proton movement and/or differences in solvent accessibility between crystallographic active sites (Fig. S2). This would be similar to the histidines found in catalytic triads of proteases, where differential protonation of one nitrogen could be tied to the protonation state of the other with the help of a SSHB interaction⁴⁹. It should be noted in the N^{δ1}-protonated active site (Fig. 5a) that the omit |F_o|-|F_c| difference density at 3.0σ for the N^{δ1}-bound proton is elongated and faces towards solvent. This may be interpreted as proton exchange with solvent. Investigating the literature for other enzymes utilizing a tyrosine-histidine pair in catalysis reveals the metalloenzyme Photosystem II (PSII) that utilizes CPETs⁵⁰. The tyrosine-histidine pair of (PSII) appears to have a SSHB that needs to be maintained for catalysis with measured pK_a values ranging between 7.3 and 8.0. For MnSOD, the Tyr166-His30 interaction is needed for catalysis though it is unclear whether the differential protonation observed at N^{δ1}(His30) is modulated with an imidazolate anion or tautomerization.

Previous mutagenesis studies suggest that the Tyr166 and His30 interaction is needed for catalysis and support the interpretation of proton transfers occurring between N^{ε2}(His30) and Oⁿ(Tyr166) that may coincide with differential protonation of N^{δ1}(His30) (Fig. 5c). To judge whether protonation of histidine is significant for enzymatic activity, site-directed mutagenesis of His → Gln is often performed due to the similar side-chain structures⁵¹. His30Gln is the only His30 mutant that has been studied that maintains the hydrogen bonding at the active site and does not significantly affect the positions of other residues at the active site^{52,53}. Kinetically, the His30Gln rate for k_1 (Mn³⁺ → Mn²⁺) is 38% of the wildtype while k_2 (Mn²⁺ → Mn³⁺) is 72%⁵⁴. The rates indicate an important role for His30 k_1 that may correspond with our observations of its differential protonation only in Mn³⁺SOD. It should be noted that previous studies refrain from

attributing differential protonations to His30 due to the similar redox potentials between wildtype (393 ± 29 mV) and His30Gln (380 ± 30 mV)^{52,53,55}. However, the investigations do not consider whether compensatory protonations or deprotonations occur at nearby residues as a result of the mutation giving the appearance of an inconsequential effect. Indeed, the Tyr34Phe mutant also has an insignificant change of redox potential (435 ± 30 mV) but has a nearly identical rate for k_1 (37% of wildtype) compared to His30Gln^{52,54}. Drawing an inference from the Tyr166Phe mutant is difficult because hydrogen bonding and side-chain conformations are significantly changed at the active site but have nearly identical measurements of redox potential (436 ± 10 mV) compared to Tyr34Phe indicating a synonymous effect to the charge of the active site^{52,54}. The neutron data for His30 and Tyr166 potentially explain past observations of MnSOD mutants and ties together changes of protonation state with kinetic and redox potential measurements.

Conclusions

In total, the present work provides details for an unusual CPET mechanism for human MnSOD. Through neutron diffraction, direct evidence is observed for (1) an internal protonation mechanism via glutamine deprotonation to the Mn-bound solvent molecule (WAT1) supported by quantum calculations, (2) a SSHB of Trp123 with the anionic form of Gln143 that stabilizes the anion (3) differentially protonated Tyr34 that interacts intimately with a solvent molecule (WAT2) when ionized, and (4) alternate protonation states for His30 that may coincide with the protonation state of Tyr166 across the dimer interface. As a result of obtaining neutron structures for both Mn^{3+} and Mn^{2+} states, we built a suggested mechanism that details the changes of protonation states as a result of the Mn gaining or losing an electron.

Starting from the resting state, five-coordinate Mn^{3+} acquires an electron (in reality from the substrate) that coincides with $\text{N}^{\delta 1}(\text{His30})$ acquiring a proton from the nearest solvent molecule (the crystallographic position of WAT2) and Tyr166 gaining a proton from $\text{N}^{\epsilon 2}(\text{His30})$ (Fig. 6a). The Mn^{2+} active site then binds ^-OH to form a six-coordinate Mn^{2+} complex (Fig. 6b). This may be the same solvent molecule that donated a proton to His30 and its binding is promoted by the electrostatics of the active site. The depression of Mn^{2+} positive charge through ^-OH binding causes negative polarization at WAT1 and triggers proton abstraction from Gln143. Consequently, the WAT1-Gln143 is more stabilizing and the electronegative polarity now localizes to OL. When the substrate is present, the steps of Fig. 6a-b describe the first CPET

where proton and electron transfers are energetically coupled to an extent where they cannot be differentiated with kinetic measurements⁴². The increase of negative character for OL may cause it to act as a better proton acceptor and to be converted to H₂O by protonation from Tyr34 as suggested by the Miller group¹⁵ (Fig 6c). Tyr34 is protonated by the solvent before its proton donation to OL. Once Tyr34 is protonated again, the second CPET may occur. The substrate would then acquire an electron from Mn²⁺ and gain two protons, one from His30 and one from Tyr34, to form the H₂O₂ product (Fig. 6d). The changes of charge due to proton and electron departure from the active site causes Gln143 to accept the same proton it previously donated to WAT1 and N^ε2(His30) accepting the proton it previously donated to Tyr166 to regenerate five-coordinate Mn³⁺.

Altogether, the suggested mechanism utilizes two “internal” proton transfers where the protons move back-and-forth within the active site and two “external” proton transfers where the protons originate from solvent molecules to ultimately be consumed to form the product. The proton transfer between WAT1 and Gln143 is especially central to the mechanism as it permits the cyclic nature of catalysis. From this study, we have revealed, to our knowledge, the first direct coupling of electronic states to protonation states for an oxidoreductase. It is evident the CPET mechanism of MnSOD is not straightforward and is exemplified by the previous elusiveness of the proton source for WAT1. Tyr34 was assumed to be the donor but our data instead indicates an unusual and unexpected proton transfer from the Gln143 amide. Likewise, Trp123, His30, and Tyr166 were not assumed to be involved in catalysis. As this is just one biologically relevant oxidoreductase in a sea of many, finding the protonation states at the active sites of other oxidoreductases may reveal further novel mechanisms for CPET.

Materials and Methods

Perdeuterated expression, purification, and crystallization. Detailed methods for recombinant MnSOD deuterated expression at ORNL biodeuteration lab, purification, and crystallization have been described previously⁵⁶. Of note, expression was performed at 37 °C instead of the 30 °C in the citation, as this significantly increases Mn metal incorporation of MnSOD⁵⁷. Purification and crystallization were performed with hydrogenated reagents. Deuterium exchange of crystals was performed by vapor diffusion in capillaries.

Redox manipulation of perdeuterated MnSOD crystals. Methods for manipulating the Mn metal of MnSOD to either Mn^{3+} or Mn^{2+} have been described previously¹⁴. In brief, a crystal in a quartz capillary was soaked in deuterated reservoir solutions containing either 6.4 mM potassium permanganate (KMnO_4) to achieve the Mn^{3+} state or 300 mM sodium hydrosulfite ($\text{Na}_2\text{S}_2\text{O}_4$) to achieve the Mn^{2+} state. After drying the crystal from soaking solutions, the crystal was flanked in the capillary by slugs of the deuterated reservoir soaking solutions. Fortuitously, the decomposition products of the redox agents are unable to enter the active site of MnSOD¹⁴.

Neutron and X-ray data collection. Data collection was preceded by the replacement of the deuterated and redox-agent containing reservoir slugs with fresh equivalents. Time-of-flight wavelength-resolved neutron Laue diffraction data were used to collect data from the 0.46 mm^3 perdeuterated crystal using the MaNDi instrument^{58,59} at the ORNL SNS using all neutrons with wavelengths between 2-4 Å. Data collection of each diffraction pattern was from the crystal held in a stationary position, with successive diffraction patterns being collected after 20° rotations along the Φ axis. A KMnO_4 -treated perdeuterated crystal of 0.46 mm^3 in volume at 296K was recorded to 2.20 Å resolution for the Mn^{3+} SOD form and subsequently treated with $\text{Na}_2\text{S}_2\text{O}_4$ to achieve the Mn^{2+} SOD state where 2.30 Å data were collected (Table S5). $\text{Na}_2\text{S}_2\text{O}_4$ is noted to deteriorate diffraction quality and was observed to increase the c unit cell axis by $\sim 1 \text{ Å}$ ¹⁴. After neutron data were collected from the crystal in the Mn^{2+} SOD state, X-ray diffraction data were collected at 296 K to 2.16 Å resolution using a Rigaku FR-E SuperBright home source. After room-temperature data collection, the crystal was not suitable for Mn^{3+} SOD data collection and a sister crystal grown from the same well was used instead for obtaining X-ray data to 1.87 Å resolution.

Data processing and refinement. Neutron data were integrated using *MANTID*⁶⁰. Integrated neutron data were scaled and wavelength-normalized using *LAUENORM* from the *LAUGEN* suite⁶¹. X-ray diffraction data were reduced using *HKL-3000* for indexing, integration, and scaling⁶². The refinement of both X-ray and neutron models was completed with *PHENIX.REFINE* from the *PHENIX* suite⁶³. The X-ray model was first refined against its corresponding data set and subsequently used as the starting model for neutron refinement. Torsional backbone angle restraints were derived from the X-ray model and applied to neutron refinement using a geometric target function with *PHENIX.REFINE*⁶³. The neutron refinement

process was performed to model the D atoms of the active site last to limit phase bias. For the initial rounds of refinement to fit protein structure, only non-exchangeable D atoms (which have stereochemical predictable positions) were present. Afterwards, each individual exchangeable position outside the active site was inspected for residual $|F_o|-|F_c|$ nuclear density and modeled with D atoms appropriately before more iterations of refinement. Next, the O atoms of solvent molecules were first modelled manually outside the active site and refined to determining whether to model solvent as O, OD, or DOD using residual $|F_o|-|F_c|$ nuclear density. The omit density peaks were also used to discern the appropriate orientation of the solvent molecules. After refinement of the solvent structure outside the active site, non-D atoms of the active site were modelled, including Mn and the O of solvent. Last, D atoms of the active site were modeled and refined manually.

Computational Details. Computational methods are discussed with further depth in the supplementary methods. All quantum mechanical (QM) DFT calculations were performed with the NWChem 6.8 software⁶⁴. The COSMO solvation model for real solvents was then implemented into the geometry optimizations to model the solution phase until an energy difference of < 0.31375 kcal/mol was reached between macro-iterations⁶⁵. The def2-TZVPD basis set was used for the Mn ion whereas the 6-31+G(d,p) Pople basis set was specifically used for all other atoms due to its use in predicting pK_{as} under the B3LYP functional^{66,67}. The QM models utilized for DFT calculations encompassed the active site residues that had the O and N atoms of the peptide backbone truncated and the C^α fixed. Additional fixed restraints were placed on aromatic residues found on the periphery of the active site (Phe66, Trp123, Trp166, and Tyr166) to mimic the packing found in the native enzyme. The Mn ion used the high-spin quintet and sextet states for trivalent and divalent systems, respectively, per experimental observations⁶⁸.

Bonding orbital analysis. The JANPA software package was used to calculate Chemist's Localized Property-optimized Orbitals (CLPOs) from open-shell DFT geometry optimizations^{34,35,69,70}. These are bonding and antibonding orbitals with maximum electron density computed through a series of localized basis set transformations. CLPOs are calculated with the same target quantity as Natural Bond Orbital (NBO) methods and yield highly comparable results^{32,33,71}. The electron delocalization stabilization/destabilization energies utilized second-order perturbation theory analysis of the Fock matrix defined by the NBO

methods⁷² but were done in the CLPO basis of JANPA. The energy associated with electron delocalization from lone pair or bonding orbital i to antibonding orbital j is defined as

$$\Delta E_{i \rightarrow j}^2 = -q_i \frac{\langle i | \hat{F} | j \rangle^2}{\langle j | \hat{F} | j \rangle - \langle i | \hat{F} | i \rangle}$$

where q_i is the donor orbital occupancy and \hat{F} is the effective orbital Hamiltonian⁷². Values $\langle j | \hat{F} | j \rangle$ and $\langle i | \hat{F} | i \rangle$ are diagonal CLPO Fock matrix elements indicative of orbital energies and $\langle i | \hat{F} | j \rangle$ is the off-diagonal matrix element representative of perturbation.

Data availability

Coordinates and structure factors for oxidized and reduced MnSOD determined with X-ray and neutron crystallography have been deposited in the Protein Data Bank (PDB 7KKS, 7KKW, 7KKU AND 7KLB). All relevant data supporting the key findings of this study are available within the article and its Supplementary Information files or from the corresponding author upon reasonable request.

References

- 1 Costentin, C., Robert, M. & Saveant, J. M. Concerted proton-electron transfers: electrochemical and related approaches. *Acc. Chem. Res.* **43**, 1019-1029, doi:10.1021/ar9002812 (2010).
- 2 Carneiro, P., Duarte, M. & Videira, A. Characterization of apoptosis-related oxidoreductases from *Neurospora crassa*. *PLoS One* **7**, e34270, doi:10.1371/journal.pone.0034270 (2012).
- 3 Chang, C. J., Chang, M. C., Damrauer, N. H. & Nocera, D. G. Proton-coupled electron transfer: a unifying mechanism for biological charge transport, amino acid radical initiation and propagation, and bond making/breaking reactions of water and oxygen. *Biochim. Biophys. Acta* **1655**, 13-28, doi:10.1016/j.bbabi.2003.08.010 (2004).
- 4 Miller, A. F., Padmakumar, K., Sorkin, D. L., Karapetian, A. & Vance, C. K. Proton-coupled electron transfer in Fe-superoxide dismutase and Mn-superoxide dismutase. *J. Inorg. Biochem.* **93**, 71-83 (2003).
- 5 Wallace, D. C. Mitochondria and cancer. *Nat. Rev. Cancer* **12**, 685-698, doi:10.1038/nrc3365 (2012).
- 6 Xu, F. Applications of oxidoreductases: Recent progress. *Industrial Biotechnology* **1**, 38-50 (2015).
- 7 Batinic-Haberle, I., Reboucas, J. S. & Spasojevic, I. Superoxide dismutase mimics: chemistry, pharmacology, and therapeutic potential. *Antioxid. Redox Signal.* **13**, 877-918, doi:10.1089/ars.2009.2876 (2010).
- 8 Perry, J. J. *et al.* Contribution of human manganese superoxide dismutase tyrosine 34 to structure and catalysis. *Biochemistry* **48**, 3417-3424, doi:10.1021/bi8023288 (2009).
- 9 Fukui, T. & Ushio-Fukai, M. Superoxide dismutases: role in redox signaling, vascular function, and diseases. *Antioxid. Redox Signal.* **15**, 1583-1606, doi:10.1089/ars.2011.3999 (2011).
- 10 Pinero, J. *et al.* DisGeNET: a comprehensive platform integrating information on human disease-associated genes and variants. *Nucleic Acids Res.* **45**, D833-D839, doi:10.1093/nar/gkw943 (2017).
- 11 Valenti, L. *et al.* The mitochondrial superoxide dismutase A16V polymorphism in the cardiomyopathy associated with hereditary haemochromatosis. *J. Med. Genet.* **41**, 946-950, doi:10.1136/jmg.2004.019588 (2004).
- 12 Azadmanesh, J., Trickel, S. R. & Borgstahl, G. E. O. Substrate-analog binding and electrostatic surfaces of human manganese superoxide dismutase. *J. Struct. Biol.* **199**, 68-75, doi:10.1016/j.jsb.2017.04.011 (2017).
- 13 O'Dell, W. B., Bodenheimer, A. M. & Meilleur, F. Neutron protein crystallography: A complementary tool for locating hydrogens in proteins. *Arch. Biochem. Biophys.* **602**, 48-60, doi:10.1016/j.abb.2015.11.033 (2016).
- 14 Azadmanesh, J., Lutz, W. E., Weiss, K. L., Coates, L. & Borgstahl, G. E. O. Redox manipulation of the manganese metal in human manganese superoxide dismutase for neutron diffraction. *Acta Cryst. F* **74**, 677-687, doi:10.1107/S2053230X18011299 (2018).
- 15 Maliekal, J. *et al.* Comparison and contrasts between the active site PKs of Mn-superoxide dismutase and those of Fe-superoxide dismutase. *J. Am. Chem. Soc.* **124**, 15064-15075 (2002).

- 16 Rulisek, L., Jensen, K. P., Lundgren, K. & Ryde, U. The Reaction Mechanism of Iron and Manganese Superoxide Dismutases Studied by Theoretical Calculations. *J. Comput. Chem.* **27** (2006).
- 17 Rulisek, L. & Ryde, U. Structure of Reduced and Oxidized Manganese Superoxide Dismutase: A Combined Computational and Experimental Approach. *J. Phys. Chem. B* **110**, 11511-11518 (2006).
- 18 Srnec, M., Aquilante, F., Ryde, U. & Rulisek, L. Reaction Mechanism of Manganese Superoxide Dismutase Studied by Combined Quantum and Molecular Mechanical Calculations and Multiconfigurational Methods. *J. Phys. Chem. B*, 6074-6086 (2009).
- 19 Han, W. G., Lovell, T. & Noodleman, L. Coupled redox potentials in manganese and iron superoxide dismutases from reaction kinetics and density functional/electrostatics calculations. *Inorg. Chem.* **41**, 205-218, doi:10.1021/ic010355z (2002).
- 20 Li, J., Fisher, C. L., Konecny, R., Bashford, D. & Noodleman, L. Density Functional and Electrostatic Calculations of Manganese Superoxide Dismutase Active Site Complexes in Protein Environments. *Inorg. Chem.* **38**, 929-939 (1999).
- 21 Noodleman, L., Lovell, T., Han, W. G., Li, J. & Himo, F. Quantum chemical studies of intermediates and reaction pathways in selected enzymes and catalytic synthetic systems. *Chem. Rev.* **104**, 459-508, doi:10.1021/cr020625a (2004).
- 22 Lah, M. S. *et al.* Structure-function in Escherichia coli iron superoxide dismutase: comparisons with the manganese enzyme from Thermus thermophilus. *Biochemistry* **34**, 1646-1660 (1995).
- 23 Heimdal, J., Kaukonen, M., Srnec, M., Rulisek, L. & Ryde, U. Reduction potentials and acidity constants of Mn superoxide dismutase calculated by QM/MM free-energy methods. *Chemphyschem* **12**, 3337-3347, doi:10.1002/cphc.201100339 (2011).
- 24 Abreu, I. A., Rodriguez, J. A. & Cabelli, D. E. Theoretical studies of manganese and iron superoxide dismutases: superoxide binding and superoxide oxidation. *J. Phys. Chem. B* **109**, 24502-24509, doi:10.1021/jp052368u (2005).
- 25 Remer, L. C. & Jensen, J. H. Toward a General Theory of Hydrogen Bonding: The Short, Strong Hydrogen Bond. *J. Phys. Chem. A* **104**, 9266-9275 (2000).
- 26 Gerlt, J. A., Kreevoy, M. M., Cleland, W. & Frey, P. A. Understanding enzymic catalysis: the importance of short, strong hydrogen bonds. *Chem. Biol.* **4**, 259-267 (1997).
- 27 Kumar, P., Agarwal, P. K. & Cuneo, M. J. On the Case of the Misplaced Hydrogens. *ChemBioChem*, doi:10.1002/cbic.202000376 (2020).
- 28 Eriksson, M. A., Hard, T. & Nilsson, L. On the pH dependence of amide proton exchange rates in proteins. *Biophys. J.* **69**, 329-339, doi:10.1016/S0006-3495(95)79905-2 (1995).
- 29 Malwal, S. R. *et al.* Catalytic Role of Conserved Asparagine, Glutamine, Serine, and Tyrosine Residues in Isoprenoid Biosynthesis Enzymes. *ACS Catal.* **8**, 4299-4312, doi:10.1021/acscatal.8b00543 (2018).
- 30 Nakamura, A. *et al.* "Newton's cradle" proton relay with amide-imidic acid tautomerization in inverting cellulase visualized by neutron crystallography. *Sci Adv* **1**, e1500263, doi:10.1126/sciadv.1500263 (2015).
- 31 Grigorenko, B. L., Khrenova, M. G. & Nemukhin, A. V. Amide-imide tautomerization in the glutamine side chain in enzymatic and photochemical reactions in proteins. *Phys. Chem. Chem. Phys.* **20**, 23827-23836, doi:10.1039/c8cp04817g (2018).

- 32 Nikolaienko, T. Y. The maximum occupancy condition for the localized property-optimized orbitals. *Phys. Chem. Chem. Phys.* **21**, 5285-5294, doi:10.1039/c8cp07276k (2019).
- 33 Glendening, E. D., Landis, C. R. & Weinhold, F. NBO 7.0: New vistas in localized and delocalized chemical bonding theory. *J. Comput. Chem.* **40**, 2234-2241, doi:10.1002/jcc.25873 (2019).
- 34 Nikolaienko, T. Y., Bulavin, L. A. & Hovorun, D. M. JANPA: An open source cross-platform implementation of the Natural Population Analysis on the Java platform. *Comput. Theor. Chem.* **1050**, 15-22.
- 35 Nikolaienko, T. Y. & Bulavin, L. A. Localized orbitals for optimal decomposition of molecular properties. *Int. J. Quantum Chem.* **119**, e25798 (2019).
- 36 Hsieh, Y. *et al.* Probing the active site of human manganese superoxide dismutase: the role of glutamine 143. *Biochemistry* **37**, 4731-4739, doi:10.1021/bi972395d (1998).
- 37 Greenleaf, W. B. *et al.* Role of hydrogen bonding in the active site of human manganese superoxide dismutase. *Biochemistry* **43**, 7038-7045, doi:10.1021/bi049888k (2004).
- 38 Cabelli, D. E. *et al.* Role of tryptophan 161 in catalysis by human manganese superoxide dismutase. *Biochemistry* **38**, 11686-11692 (1999).
- 39 Hearn, A. S. *et al.* Kinetic analysis of product inhibition in human manganese superoxide dismutase. *Biochemistry* **40**, 12051-12058 (2001).
- 40 Guan, Y. *et al.* Crystal structure of Y34F mutant human mitochondrial manganese superoxide dismutase and the functional role of tyrosine 34. *Biochemistry* **37**, 4722-4730, doi:10.1021/bi972394l (1998).
- 41 Sheng, Y. *et al.* Superoxide dismutases and superoxide reductases. *Chem. Rev.* **114**, 3854-3918, doi:10.1021/cr4005296 (2014).
- 42 Hsu, J. L. *et al.* Catalytic properties of human manganese superoxide dismutase. *J. Biol. Chem.* **271**, 17687-17691, doi:10.1074/jbc.271.30.17687 (1996).
- 43 Michalczyk, R. *et al.* Joint neutron crystallographic and NMR solution studies of Tyr residue ionization and hydrogen bonding: Implications for enzyme-mediated proton transfer. *Proc. Natl. Acad. Sci. U. S. A.* **112**, 5673-5678, doi:10.1073/pnas.1502255112 (2015).
- 44 MacMillan-Crow, L. A. & Thompson, J. A. Tyrosine modifications and inactivation of active site manganese superoxide dismutase mutant (Y34F) by peroxynitrite. *Arch. Biochem. Biophys.* **366**, 82-88, doi:10.1006/abbi.1999.1202 (1999).
- 45 Borgstahl, G. E. O., Pokross, M., Chehab, R., Sekher, A. & Snell, E. H. Cryo-trapping the six-coordinate, distorted-octahedral active site of manganese superoxide dismutase. *J. Mol. Biol.* **296**, 951-959, doi:10.1006/jmbi.1999.3506 (2000).
- 46 Porta, J., Vahedi-Faridi, A. & Borgstahl, G. E. O. Structural analysis of peroxide-soaked MnSOD crystals reveals side-on binding of peroxide to active-site manganese. *J. Mol. Biol.* **399**, 377-384, doi:10.1016/j.jmb.2010.04.031 (2010).
- 47 Whittaker, M. M. & Whittaker, J. W. Low-temperature thermochromism marks a change in coordination for the metal ion in manganese superoxide dismutase. *Biochemistry* **35**, 6762-6770, doi:10.1021/bi960088m (1996).
- 48 Walba, H. & Isensee, R. W. Acidity Constants of Some Arylimidazoles and Their Cations. *J. Org. Chem.* **26**, 2789-2791 (1961).
- 49 Dodson, G. & Wlodawer, A. Catalytic triads and their relatives. *Trends Biochem. Sci.* **23**, 347-352, doi:10.1016/s0968-0004(98)01254-7 (1998).

- 50 Styring, S., Sjöholm, J. & Mamedov, F. Two tyrosines that changed the world: Interfacing the oxidizing power of photochemistry to water splitting in photosystem II. *Biochim. Biophys. Acta* **1817**, 76-87, doi:10.1016/j.bbapap.2011.03.016 (2012).
- 51 Ehrig, T., Hurley, T. D., Edenberg, H. J. & Bosron, W. F. General base catalysis in a glutamine for histidine mutant at position 51 of human liver alcohol dehydrogenase. *Biochemistry* **30**, 1062-1068, doi:10.1021/bi00218a026 (1991).
- 52 Hearn, A. S. *et al.* Amino acid substitution at the dimeric interface of human manganese superoxide dismutase. *J. Biol. Chem.* **279**, 5861-5866, doi:10.1074/jbc.M311310200 (2004).
- 53 Hearn, A. S. *et al.* Catalytic and structural effects of amino acid substitution at histidine 30 in human manganese superoxide dismutase: insertion of valine C gamma into the substrate access channel. *Biochemistry* **42**, 2781-2789, doi:10.1021/bi0266481 (2003).
- 54 Abreu, I. A. & Cabelli, D. E. Superoxide dismutases—a review of the metal-associated mechanistic variations. *Biochim. Biophys. Acta* **1804**, 263-274, doi:10.1016/j.bbapap.2009.11.005 (2010).
- 55 Leveque, V. J., Vance, C. K., Nick, H. S. & Silverman, D. N. Redox properties of human manganese superoxide dismutase and active-site mutants. *Biochemistry* **40**, 10586-10591 (2001).
- 56 Azadmanesh, J., Trickle, S. R., Weiss, K. L., Coates, L. & Borgstahl, G. E. O. Preliminary neutron diffraction analysis of challenging human manganese superoxide dismutase crystals. *Acta Cryst. F* **73**, 235-240, doi:10.1107/S2053230X17003508 (2017).
- 57 Whittaker, M. M. & Whittaker, J. W. Metallation state of human manganese superoxide dismutase expressed in *Saccharomyces cerevisiae*. *Arch. Biochem. Biophys.* **523**, 191-197, doi:10.1016/j.abb.2012.04.016 (2012).
- 58 Coates, L. *et al.* The Macromolecular Neutron Diffractometer MaNDi at the Spallation Neutron Source. *J. Appl. Crystallogr.* **48**, 1302-1306 (2015).
- 59 Coates, L., Stoica, A. D., Hoffmann, C., Richards, J. & Cooper, R. The macromolecular neutron diffractometer (MaNDi) at the Spallation Neutron Source, Oak Ridge: enhanced optics design, high-resolution neutron detectors and simulated diffraction. *J. Appl. Crystallogr.* **43**, 570-577 (2010).
- 60 Sullivan, B. *et al.* BraggNet: integrating Bragg peaks using neural networks. *J. Appl. Crystallogr.* **52**, 854-863, doi:10.1107/S1600576719008665 (2019).
- 61 Campbell, J. W. LAUEGEN, an X-windows-based program for the processing of Laue diffraction data. *J. Appl. Crystallogr.* **28**, 228-236 (1995).
- 62 Minor, W., Cymborowski, M., Otwinowski, Z. & Chruszcz, M. HKL-3000: the integration of data reduction and structure solution—from diffraction images to an initial model in minutes. *Acta Cryst. D* **62**, 859-866, doi:10.1107/S0907444906019949 (2006).
- 63 Afonine, P. V. *et al.* Towards automated crystallographic structure refinement with phenix.refine. *Acta Cryst. D* **68**, 352-367, doi:10.1107/S0907444912001308 (2012).
- 64 Valiev, M. *et al.* NWChem: A comprehensive and scalable open-source solution for large scale molecular simulation. *Comput. Phys. Commun.* **181**, 1477-1489 (2010).
- 65 Klamt, A. Conductor-like Screening Model for Real Solvents: A New Approach to the Quantitative Calculation of Solvation Phenomena. *J. Phys. Chem.* **99**, 2224-2235 (1995).
- 66 Thapa, B. & Schlegel, H. B. Density Functional Theory Calculation of pKa's of Thiols in Aqueous Solution Using Explicit Water Molecules and the Polarizable Continuum Model. *J. Phys. Chem. A* **120**, 5726-5735, doi:10.1021/acs.jpca.6b05040 (2016).

- 67 Zhang, S., Baker, J. & Pulay, P. A reliable and efficient first principles-based method for predicting pK(a) values. 1. Methodology. *J. Phys. Chem. A* **114**, 425-431, doi:10.1021/jp9067069 (2010).
- 68 Vance, C. K. & Miller, A. F. Novel insights into the basis for Escherichia coli superoxide dismutase's metal ion specificity from Mn-substituted FeSOD and its very high E(m). *Biochemistry* **40**, 13079-13087, doi:10.1021/bi0113317 (2001).
- 69 Nikolaienko, T. Y., Chuiko, V. S. & Bulavin, L. A. The dataset of covalent bond lengths resulting from the first-principle calculations. *Comput. Theor. Chem.* **1163**, 112508 (2019).
- 70 Nikolaienko, T. Y., Bulavin, L. A. & Hovorun, D. M. Can we treat ab initio atomic charges and bond orders as conformation-independent electronic structure descriptors? *RSC Advances* **6**, 74785-74796 (2016).
- 71 Nikolaienko, T. Y., S., K. E. & Dolgonos, G. A. On the Existence of He-He Bond in the Endohedral Fullerene He₂@ C₆₀. *J. Comput. Chem.* **39**, 1090-1102 (2018).
- 72 Reed, A. E., Curtiss, L. A. & Weinhold, F. Intermolecular interactions from a natural bond orbital, donor-acceptor viewpoint. *Chem. Rev.* **88**, 899-926 (1988).

Acknowledgments

We would like to thank Dr. Tymofii Y. Nikolaienko for his support in orbital analysis and utilization of the JANPA software as well as Jeffrey L. Lovelace for his computational aid. We thank Scott R. Trickle and Calor Kolar for useful discussions and technical assistance. This research was supported by NASA EPSCoR funding (44-0307-1021-201). The UNMC Structural Biology Core Facility was funded by the following National Institutes of Health (NIH) grants: the Fred and Pamela Buffett Cancer Center Support Grant (P30CA036727), National Center for Research Resources grant 5P20RR016469 and National Institute for General Medical Science grant 8P20GM103427. The research at Oak Ridge National Laboratory (ORNL) Spallation Neutron Source was sponsored by the Scientific User Facilities Division, Office of Basic Energy Sciences, US Department of Energy. This research used resources at the Second Target Station, which is a DOE Office of Science User Facilities Construction Project at ORNL. The Office of Biological and Environmental Research supported research at ORNL Center for Structural Molecular Biology (CSMB) using facilities supported by the Scientific User Facilities Division, Office of Basic Energy Sciences, US Department of Energy. Quantum computations were completed utilizing the Holland Computing Center of the University of Nebraska, which receives support from the Nebraska Research Initiative. The authors declare no competing financial interests.

Author Contributions

J.A., W.E.L., L. C., K.L.W., and G.E.O.B. performed experiments, and analyzed data. J.A. and G. E.O.B wrote the manuscript with input from all authors.

Competing interests

The authors declare no competing interests.

Supplementary information

A supplementary file of information is included.

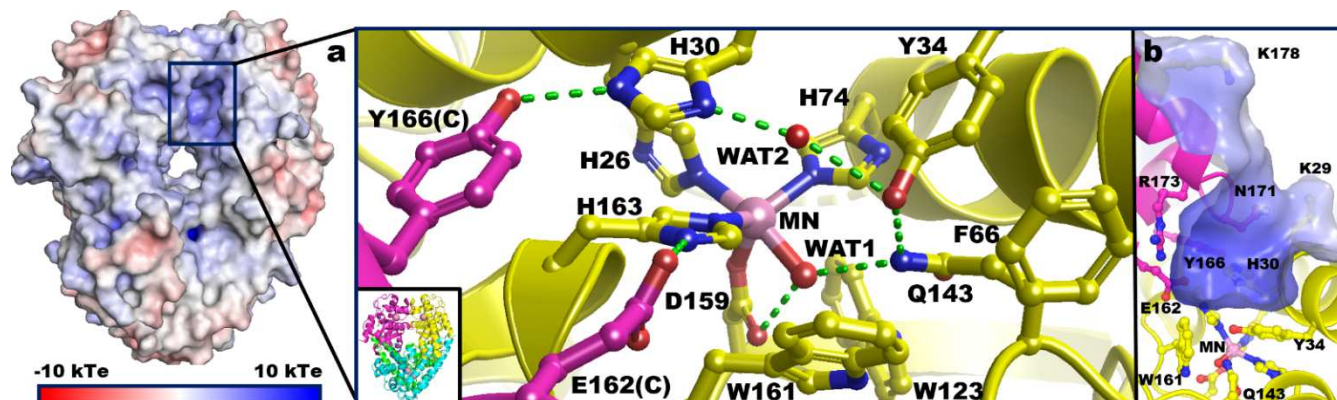


Figure 1. Structure of tetrameric human MnSOD (PDB ID 5VF9)¹². **(a)** The active site of MnSOD is within a positively-charged cavity formed from two adjacent subunits. The hydrogen bond network is denoted by green dashes and involves residues from both subunits. Solvent and substrate accessibility is possible only through the ~ 5 Å gap between His30 and Tyr34. **(b)** Side-view of the active site cavity rotated approximately 90° relative to **(a)**.

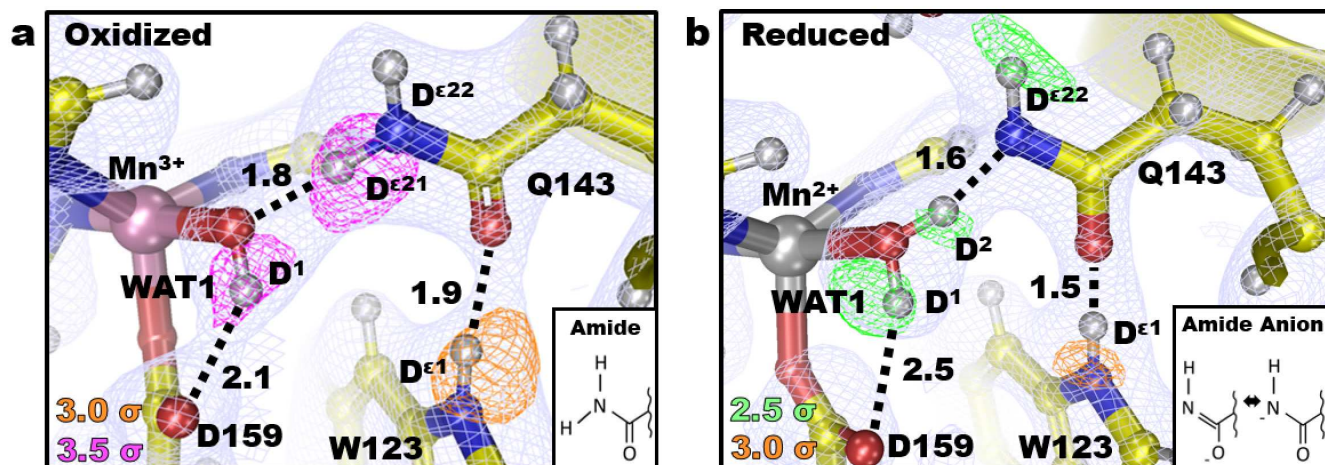


Figure 2. Proton transfer between Gln143 and the Mn-ligated solvent molecule WAT1. (a) Neutron structure at the active site of Mn³⁺SOD with magenta and orange omit $|F_o|-|F_c|$ difference nuclear density displayed at 3.5σ and 3.0σ , respectively, and light blue $2|F_o|-|F_c|$ nuclear density displayed at 1.0σ . Mn scatters negatively and therefore lacks nuclear density. Numbers are distances in Å. (b) Neutron structure at the active site of Mn²⁺SOD with green omit $|F_o|-|F_c|$ difference nuclear density displayed at 2.5σ and light blue $2|F_o|-|F_c|$ nuclear density displayed at 1.0σ . Representations of the amide and amide anions are included.

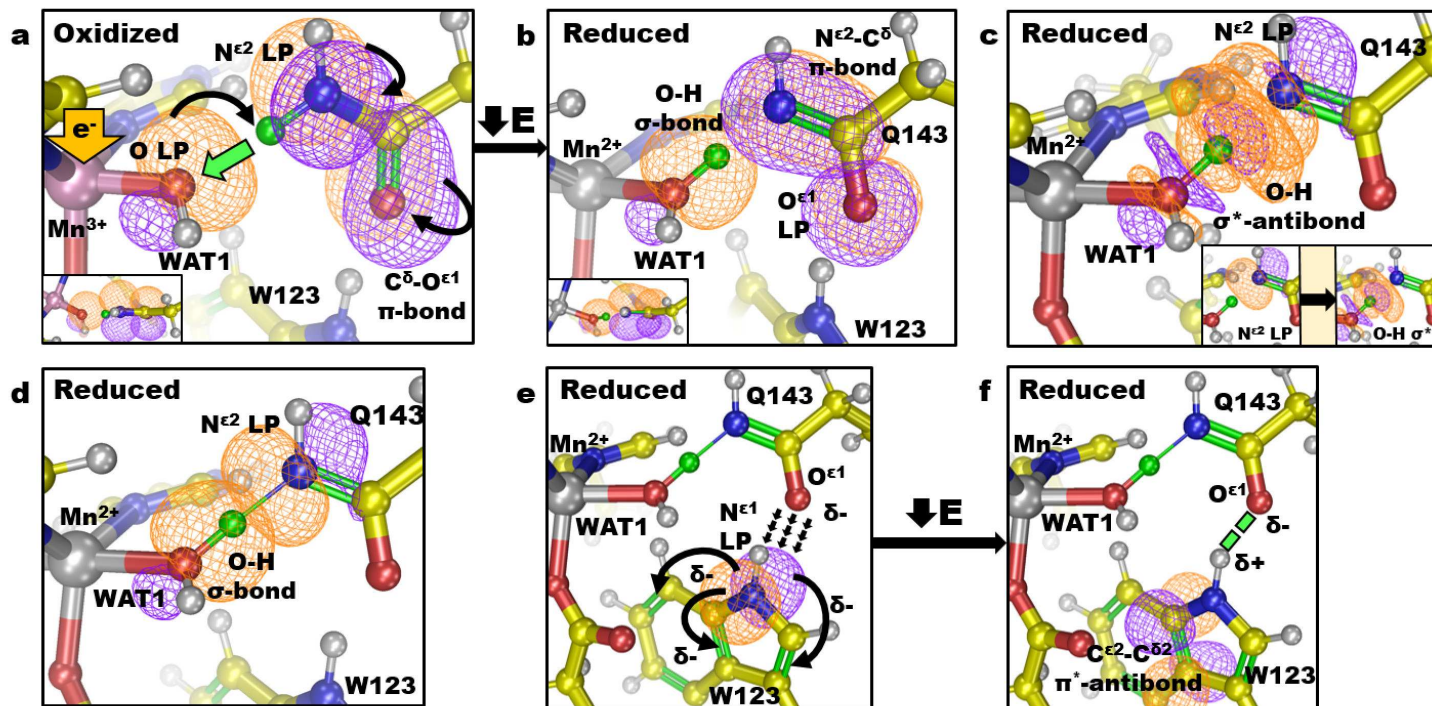


Figure 3. The suggested mechanism of Gln143 → WAT1 proton transfer utilizing bonding orbitals and optimal resonance structure calculated from DFT and subsequent CLPO analysis of the neutron structures. Orange and purple contours indicate the positive and negative orbital wave functions, respectively. Curved arrows represent electron pushing. **(a-b)** Reduction of Mn^{3+} to Mn^{2+} instigates a strong covalent need for the exposed lone pair (denoted LP) of $\text{O}^{\ominus}\text{H}(\text{WAT1})$. This is chemically remediated by the acquisition of a proton (green atom) from the proximal Gln143 amide. The dominant resonance structure of the amide anion is with a $\text{N}^{\epsilon 2}\text{-C}^{\delta 1}$ double bond as a result of $\text{N}^{\epsilon 2}$ LP delocalization from **(a)**. **(c)** Despite proton donation to WAT1, Gln143 still demonstrates covalent character with the proton (green atom). The new $\text{N}^{\epsilon 2}$ LP participates in electron density transfer to the σ^* -antibonding orbital of $\text{O-H}(\text{WAT1})$. Donor acceptor orbital analysis calculates a stabilizing energy of 1.4 kcal/mol for this hyperconjugated interaction. The inset in the lower-right corner illustrates individual orbital representations. **(d)** Due to the hyperconjugation illustrated in **(c)**, the hydrogen bond between $\text{N}^{\epsilon 2}(\text{Gln143})$ and $\text{O-H}(\text{WAT1})$ has partial σ -bonding character contributing to and increasing the strength of the hydrogen bond characteristic of SSHBs. CLPO calculations suggest the proton is covalently shared between WAT1 and Gln143, with percentages of 64% and 36%, respectively. **(e-f)** The increased electronegative character of $\text{O}^{\epsilon 1}$ electrostatically polarizes Trp123. This is achieved through the stabilizing delocalization of the $\text{N}^{\epsilon 1}(\text{Trp123})$ LP into the highly-conjugated ring. The

major stabilizing interaction decreases energy by 13.52 kcal/mol and is the donation of electron density from the $N^{\epsilon 1}$ (Trp123) LP into the adjacent $C^{\epsilon 2}$ - $C^{\delta 2}$ π^* -antibonding orbital. The polarization of Trp123 allows a SSHB between Gln143 and Trp denoted by the green dashes. The hyperconjugation and polarization of Trp123 are thought to contribute to the stability of the amide anion.

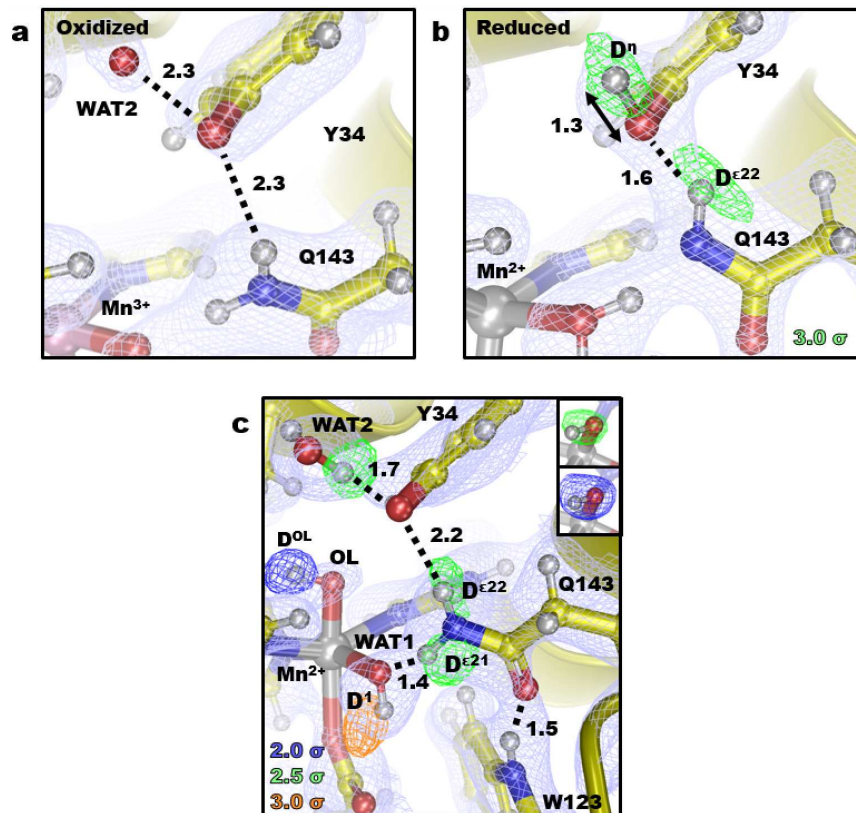


Figure 4. Differential protonations and active site coordination of MnSOD. Light blue $2|F_o|-|F_c|$ nuclear density is displayed at 1.0σ . **(a-b)** Neutron structures of five-coordinate Mn^{3+} SOD and Mn^{2+} SOD. Green omit $|F_o|-|F_c|$ difference nuclear density is at 3.0σ . **(c)** Six-coordinate Mn^{2+} SOD active site with green omit $|F_o|-|F_c|$ difference density displayed at 2.0σ , 2.5σ , and 3.0σ for blue, green, and orange contours, respectively. $|F_o|-|F_c|$ difference density is for individual D atoms except for the upper-right corner that is for both atoms of OL. Numbers are distances in Å.

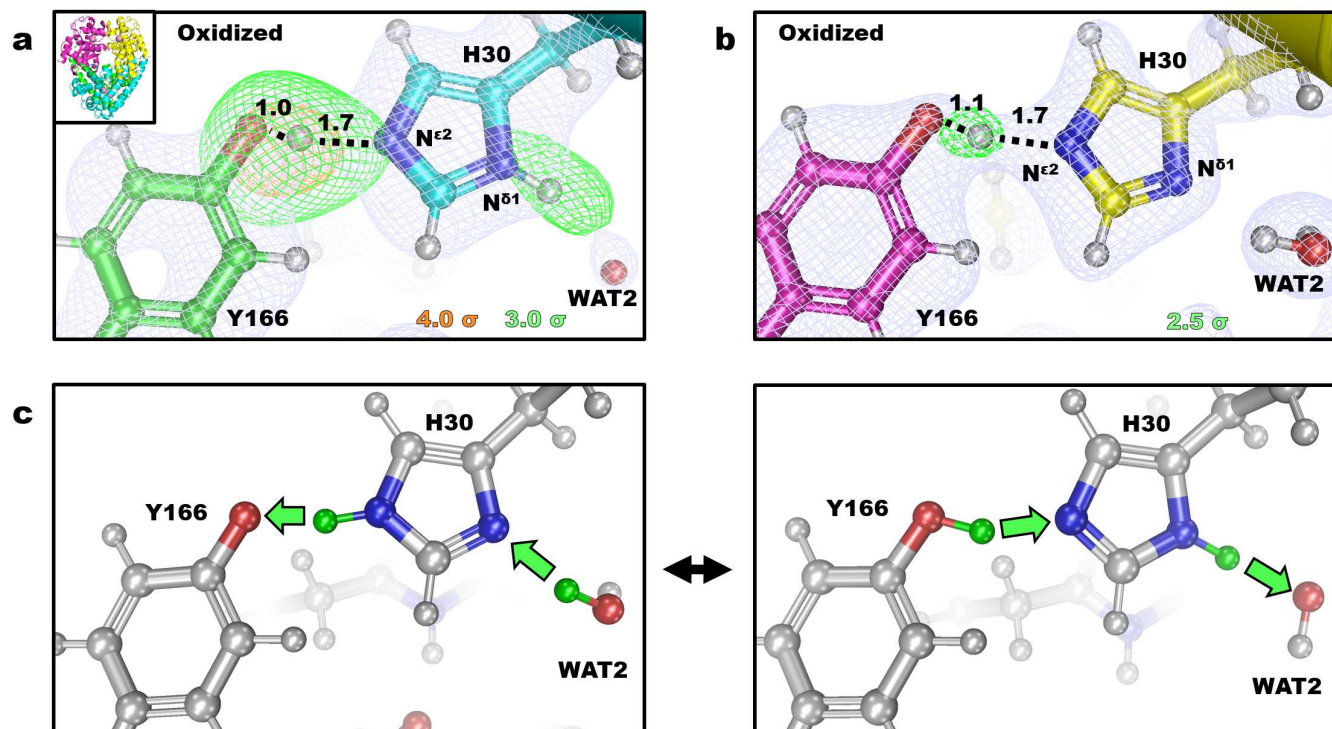


Figure 5. Differential protonation states of His30 and Tyr166 for Mn³⁺SOD. Numbers are distances in Å. (a-b) All-atom structures for the different chains of Mn³⁺SOD. Light blue $2|F_o| - |F_c|$ nuclear density displayed at 1.0σ . Green and orange omit $|F_o| - |F_c|$ difference density are displayed at contours denoted at the bottom right of the panel. (c) A suggested mechanism for differential protonation for Tyr166 and His30.

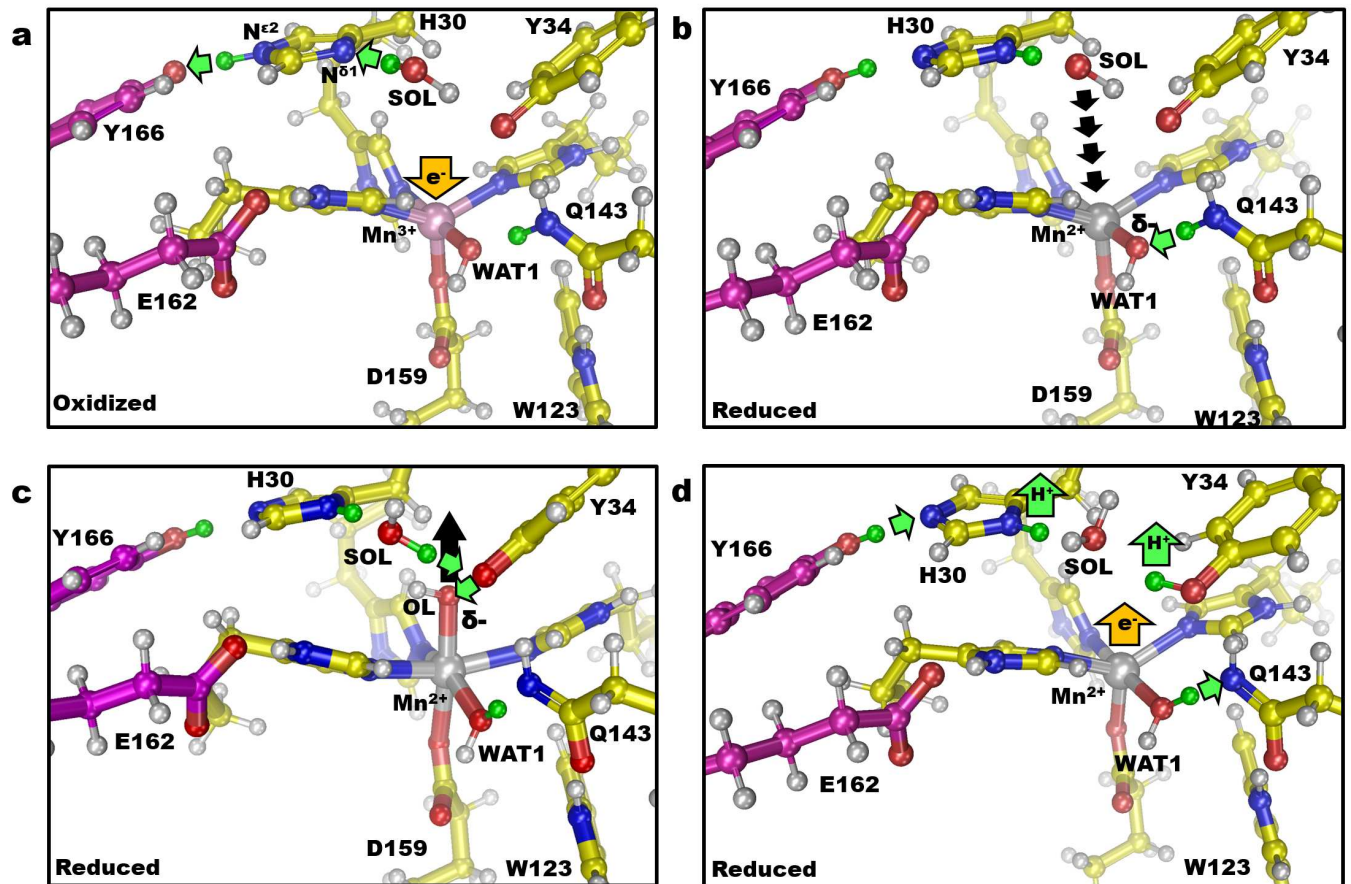


Figure 6. A suggested mechanism for MnSOD-active site proton transfers that coincide with electron gain or loss at the Mn. Solvent and substrate enter the active site through His30 and Tyr34. SOL represents the closest free solvent molecule typically found at the crystallographic site of WAT2 and is replenished from bulk solvent upon enzymatic use. (a) The thick orange arrow indicates the acquisition of an electron by Mn^{3+} which is coupled to both $N^{\delta 1}$ (His30) proton gain from solvent and $N^{\epsilon 2}$ (His30) proton donation to buried Tyr166. The direction of proton transfer is indicated by small green arrows. (b) Driven by the new electrostatic environment, a ^-OH molecule binds sixth-coordinate to Mn^{2+} as indicated by short black arrows. This suppresses the positive charge of Mn^{2+} and polarizes WAT1 to become more negative (δ^-) and instigate proton gain from Gln143 by its deprotonation. (c) The protonation at WAT1 causes electronegative polarity to instead be localized to the bound ^-OH ligand, OL. OL is subsequently protonated and departs from the active site. (d) Electron loss by substrate depicted by the orange arrow coincides with the loss of protons at His30 and Tyr34 that are presumed to be acquired by

the substrate. Tyr166 and WAT1 donate protons to His30 and Gln143, respectively, because of the net charge changes to regenerate the state in (a).

Figures

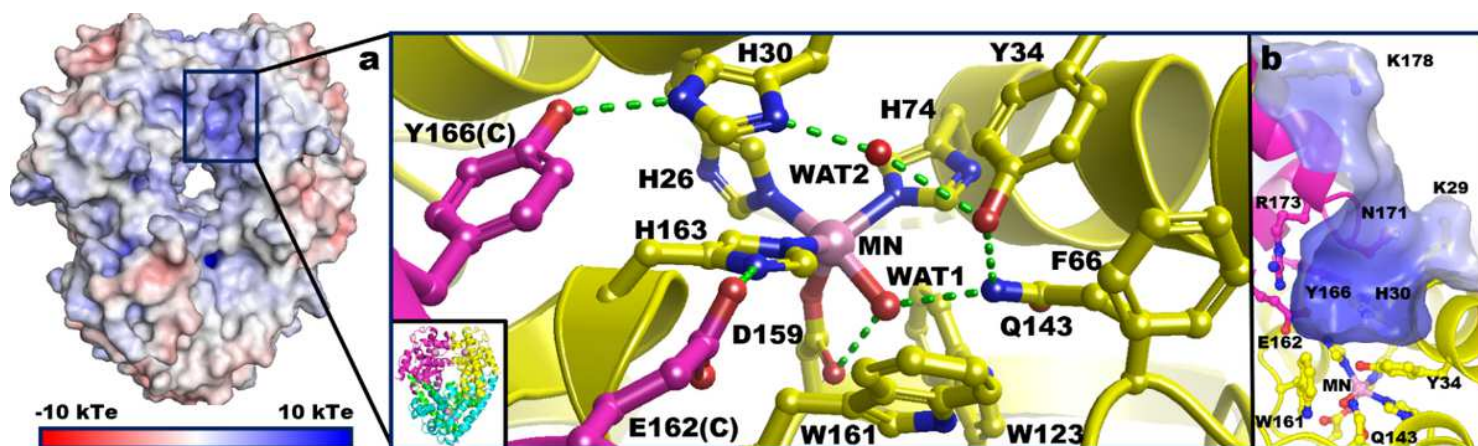


Figure 1

Structure of tetrameric human MnSOD (PDB ID 5VF9)12. (a) The active site of MnSOD is within a positively-charged cavity formed from two adjacent subunits. The hydrogen bond network is denoted by green dashes and involves residues from both subunits. Solvent and substrate accessibility is possible only through the ~ 5 Å gap between His30 and Tyr34. (b) Side-view of the active site cavity rotated approximately 90° relative to (a).

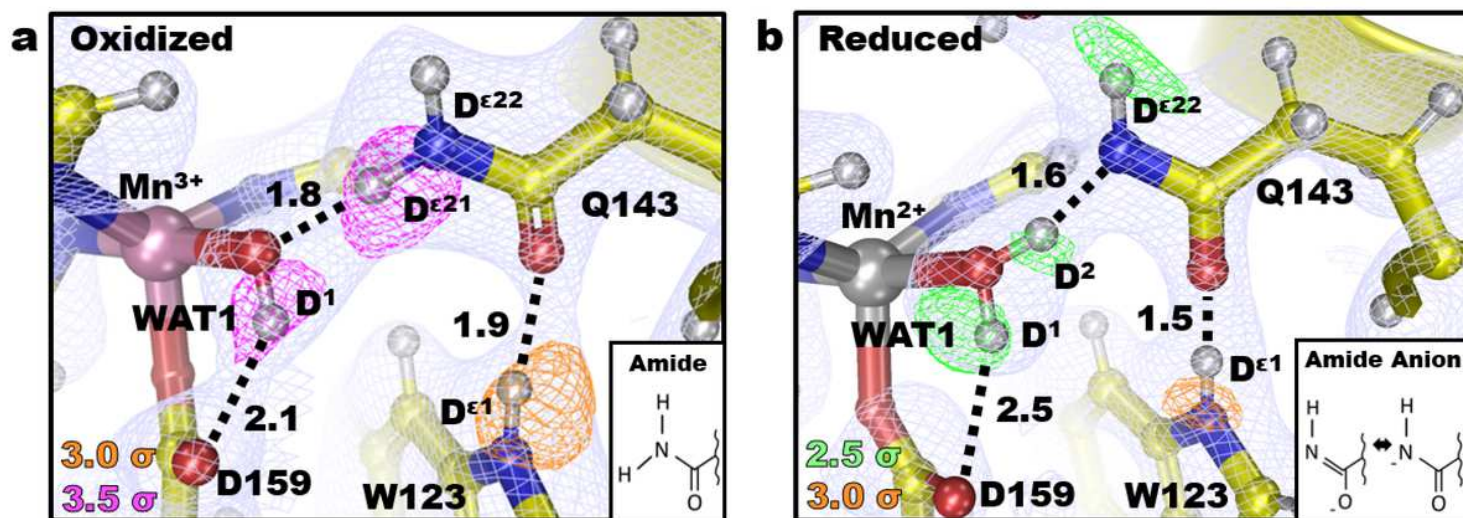


Figure 2

Proton transfer between Gln143 and the Mn-ligated solvent molecule WAT1. (a) Neutron structure at the active site of Mn³⁺-SOD with magenta and orange omit $|F_o|-|F_c|$ difference nuclear density displayed at 3.5σ and 3.0σ , respectively, and light blue $2|F_o|-|F_c|$ nuclear density displayed at 1.0σ . Mn scatters negatively and therefore lacks nuclear density. Numbers are distances in Å. (b) Neutron structure at the active site of Mn²⁺-SOD with green omit $|F_o|-|F_c|$ difference nuclear density displayed at 2.5σ and light blue $2|F_o|-|F_c|$ nuclear density displayed at 1.0σ . Representations of the amide and amide anions are included.

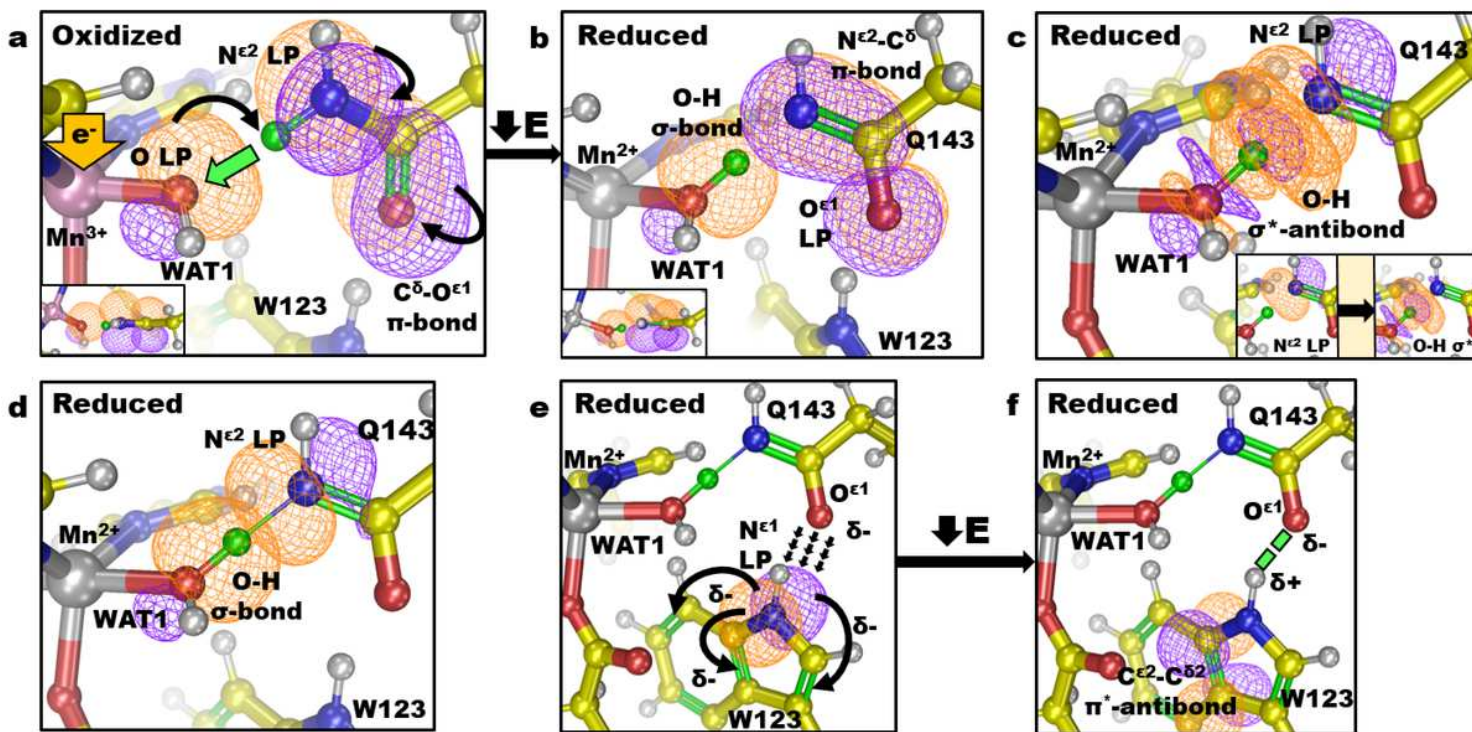


Figure 3

The suggested mechanism of Gln143 \leftrightarrow WAT1 proton transfer utilizing bonding orbitals and optimal resonance structure calculated from DFT and subsequent CLPO analysis of the neutron structures. Orange and purple contours indicate the positive and negative orbital wave functions, respectively. Curved arrows represent electron pushing. (a-b) Reduction of Mn³⁺ to Mn²⁺ instigates a strong covalent need for the exposed lone pair (denoted LP) of -OH(WAT1). This is chemically remediated by the acquisition of a proton (green atom) from the proximal Gln143 amide. The dominant resonance structure of the amide anion is with a N ϵ 2-C ϵ 1 double bond as a result of N ϵ 2 LP delocalization from (a). (c) Despite proton donation to WAT1, Gln143 still demonstrates covalent character with the proton (green atom). The new N ϵ 2 LP participates in electron density transfer to the σ^* -antibonding orbital of O-H(WAT1). Donor acceptor orbital analysis calculates a stabilizing energy of 1.4 kcal/mol for this hyperconjugated interaction. The inset in the lower-right corner illustrates individual orbital representations. (d) Due to the hyperconjugation illustrated in (c), the hydrogen bond between N ϵ 2(Gln143) and O-H(WAT1) has partial σ -bonding character contributing to and increasing the strength of the hydrogen bond characteristic of SSHBs. CLPO calculations suggest the proton is covalently shared between WAT1 and Gln143, with percentages of 64% and 36%, respectively. (e-f) The increased electronegative character of O ϵ 1 electrostatically polarizes Trp123. This is achieved through the stabilizing delocalization of the N ϵ 1(Trp123) LP into the highly-conjugated ring. The major stabilizing interaction decreases energy by 13.52 kcal/mol and is the donation of electron density from the N ϵ 1(Trp123) LP into the adjacent C ϵ 2-C δ 2 π^* -antibonding orbital. The polarization of Trp123 allows a SSHB between Gln143 and Trp denoted by the green dashes. The hyperconjugation and polarization of Trp123 are thought to contribute to the stability of the amide anion.

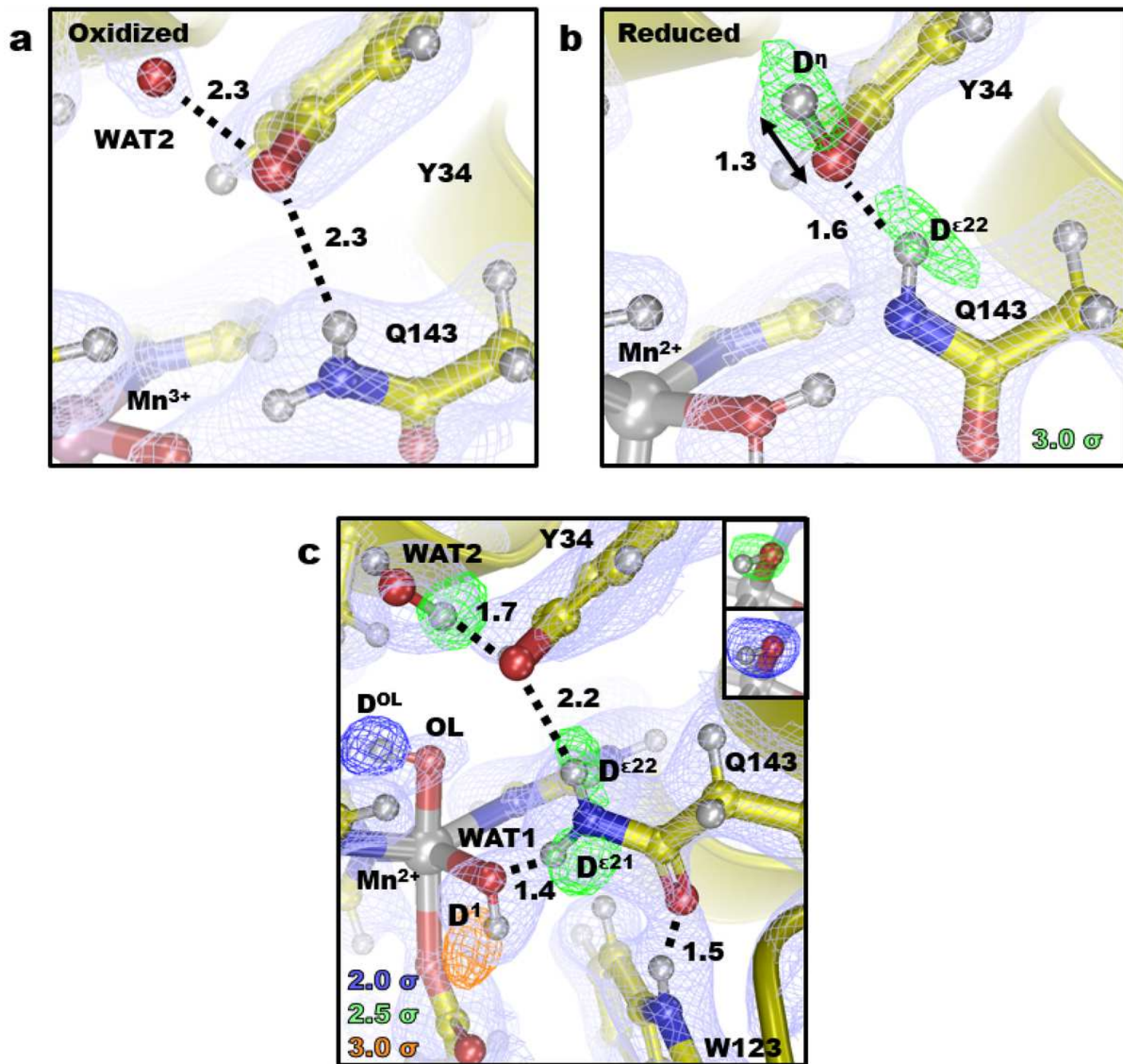


Figure 4

Differential protonations and active site coordination of MnSOD. Light blue $2|Fo|-|Fc|$ nuclear density is displayed at 1.0σ . (a-b) Neutron structures of five-coordinate Mn^{3+} SOD and Mn^{2+} SOD. Green omit $|Fo|-|Fc|$ difference nuclear density is at 3.0σ . (c) Six-coordinate Mn^{2+} SOD active site with green omit $|Fo|-|Fc|$ difference density displayed at 2.0σ , 2.5σ , and 3.0σ for blue, green, and orange contours, respectively. $|Fo|-|Fc|$ difference density is for individual D atoms except for the upper-right corner that is for both atoms of OL. Numbers are distances in Å.

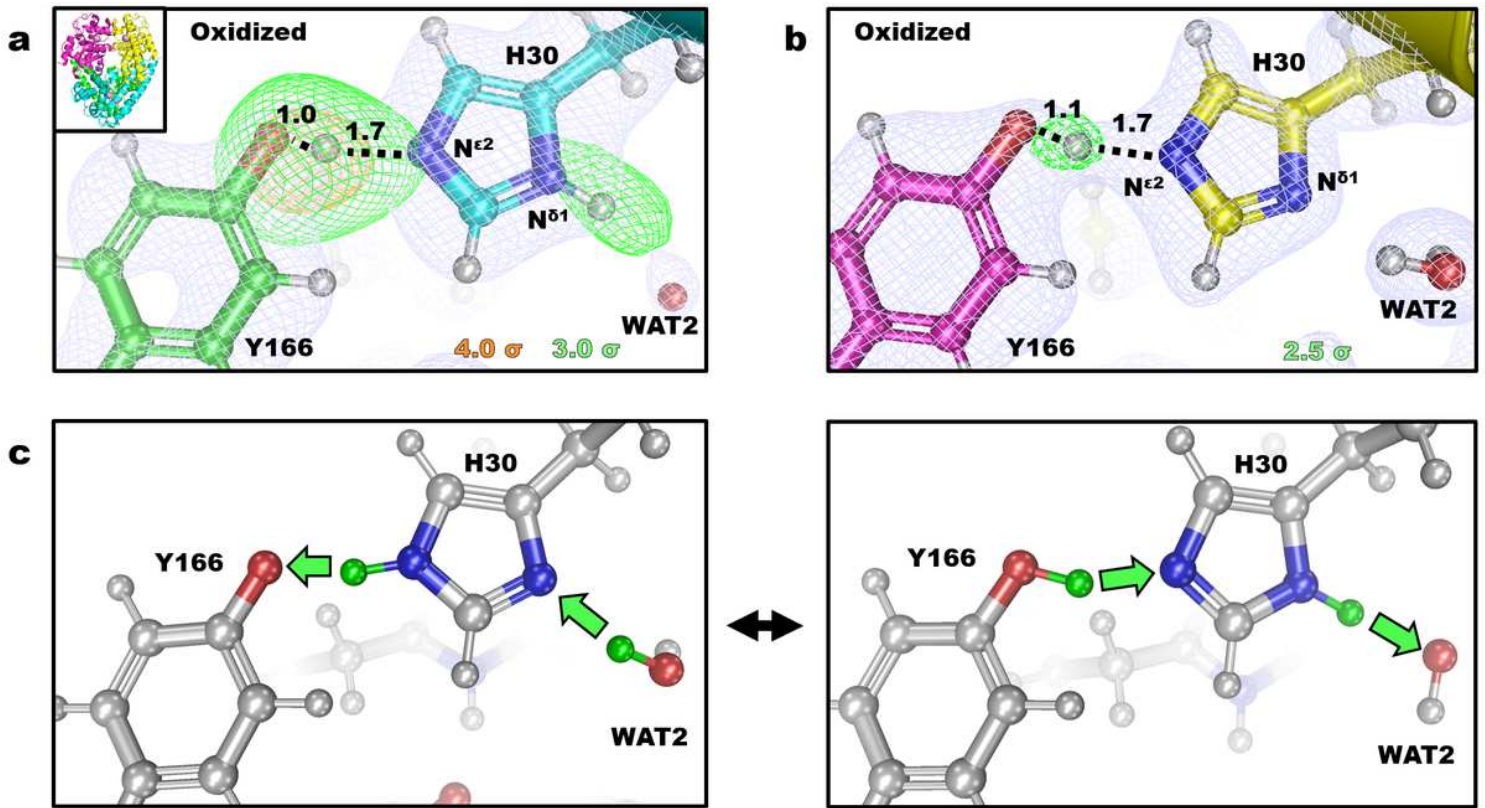


Figure 5

Differential protonation states of His30 and Tyr166 for Mn³⁺SOD. Numbers are distances in Å. (a-b) All-atom structures for the different chains of Mn³⁺SOD. Light blue 2|Fo|-|Fc| nuclear density displayed at 1.0 σ . Green and orange omit |Fo|-|Fc| difference density are displayed at contours denoted at the bottom right of the panel. (c) A suggested mechanism for differential protonation for Tyr166 and His30.

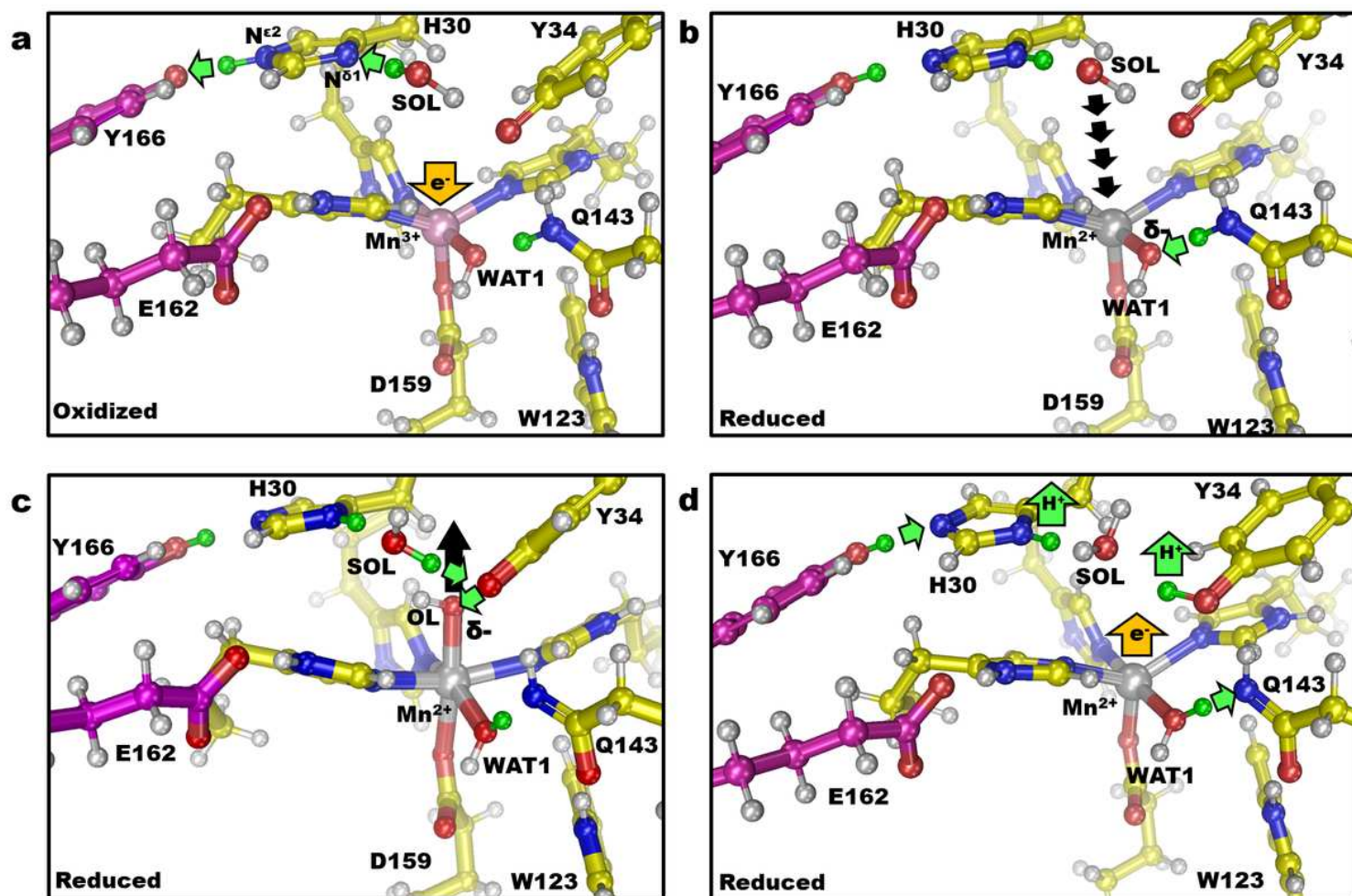


Figure 6

A suggested mechanism for MnSOD-active site proton transfers that coincide with electron gain or loss at the Mn. Solvent and substrate enter the active site through His30 and Tyr34. SOL represents the closest free solvent molecule typically found at the crystallographic site of WAT2 and is replenished from bulk solvent upon enzymatic use. (a) The thick orange arrow indicates the acquisition of an electron by Mn³⁺ which is coupled to both N δ 1(His30) proton gain from solvent and N ϵ 2(His30) proton donation to buried Tyr166. The direction of proton transfer is indicated by small green arrows. (b) Driven by the new electrostatic environment, a -OH molecule binds sixth-coordinate to Mn²⁺ as indicated by short black arrows. This suppresses the positive charge of Mn²⁺ and polarizes WAT1 to become more negative (δ^-) and instigate proton gain from Gln143 by its deprotonation. (c) The protonation at WAT1 causes electronegative polarity to instead be localized to the bound -OH ligand, OL. OL is subsequently protonated and departs from the active site. (d) Electron loss by substrate depicted by the orange arrow coincides with the loss of protons at His30 and Tyr34 that are presumed to be acquired by the substrate. Tyr166 and WAT1 donate protons to His30 and Gln143, respectively, because of the net charge changes to regenerate the state in (a).

Supplementary Files

This is a list of supplementary files associated with this preprint. Click to download.

- [110120supplement.docx](#)